

This manuscript has been authored by UT-Battelle, LLC under Contract No. DE-AC05-00OR22725 with the U.S. Department of Energy. The United States Government retains and the publisher, by accepting the article for publication, acknowledges that the United States Government retains a non-exclusive, paid-up, irrevocable, worldwide license to publish or reproduce the published form of this manuscript, or allow others to do so, for United States Government purposes. The Department of Energy will provide public access to these results of federally sponsored research in accordance with the DOE Public Access Plan (<http://energy.gov/downloads/doe-public-access-plan>).

Investigating the deformation mechanisms of a highly metastable high entropy alloy using in-situ neutron diffraction

M. Frank^a, Y. Chen^b, S.S. Nene^a, S. Sinha^a, K. Liu^a, K. An^b, R.S. Mishra^a

^aCenter for Friction Stir Processing, Department of Materials Science and Engineering, University of North Texas, Denton, Texas 76207 USA

^bNeutron Scattering Division, Oak Ridge National Laboratory, Oak Ridge, Tennessee, 37830 USA

*Corresponding author: Rajiv.Mishra@unt.edu

Abstract

The present study correlates the effect of enhanced metastability on both stacking fault energy (SFE) and deformation mechanisms in metastable high entropy alloys (HEAs). We determine the SFE of Fe₄₀Mn₂₀Cr₁₅Co₂₀Si₅ (CS-HEA) to be ~5.24 mJ m⁻² using in-situ neutron diffraction. The relatively low-measured SFE of CS-HEA results in a unique combination of fine grain size (~6 μm) and predominantly of the ε-h.c.p. phase (58%) after thermomechanical processing. We observe significant stress partitioning to the ε-h.c.p. phase during deformation, resulting in a marginal fraction of γ-f.c.c. → ε-h.c.p. transformation (~25%). An applied tensile stress induces significant lattice reorientation and decrease of the axial ratio (from ~1.619 to 1.597 Å) in the hexagonal phase. Decreases in both the axial ratio and c-axis lattice parameter suggests changes in Schmidt factor occur during deformation. The concurrent deformation twinning and pyramidal lead to high work hardenability demonstrating the benefit of metastable.

1. Introduction

Recently, metastable HEAs have exploited the composition dependence of stacking fault energy (SFE) to activate deformation-induced twinning in the f.c.c. phase (TWIP), deformation-induced γ -f.c.c. \rightarrow ϵ -h.c.p. transformation (TRIP) and deformation-induced twinning in the h.c.p phase. The result of this composition dependence has led to alloys with desirable combinations of work hardenability [1–3], elastic stiffness [4], fatigue resistance [5,6] and corrosion resistance [7]. Ultimately, increasing metastability by compositional design has led to enhanced properties. As metastability is increased the free energy difference between the γ -f.c.c. and ϵ -h.c.p. phases ($\Delta G^{\gamma \rightarrow \epsilon}$) decreases and larger phase fractions of the ϵ -h.c.p. phase are observed. Although stabilization of the ϵ -h.c.p. phase has led to enhance properties, there have been few reports aimed at design of more metastable alloys. Consequently, the effect of having a highly metastable γ -f.c.c. phase as it relates to deformation behavior remains unanswered. Furthermore, a link between further increased metastability of the γ -f.c.c. phase to both measured stacking fault energy (SFE) and deformation behavior in metastable HEAs is lacking. Considering the well-known relationship between SFE and the deformation behavior of f.c.c. metals, the need to understand the relationship between a high metastability γ -f.c.c. phase with both the SFE and deformation response is of importance.

Successful measurement of SFE has been carried out and correlated with the deformation behavior of multiple HEAs, using the transmission electron microscope (TEM) [8–10] or in-situ neutron diffraction [11]. Important to relating SFE with deformation behavior, in-situ diffraction experiments allow for concurrent evaluation of both mechanical response and microstructural evolution while determining the SFE of a bulk specimen. For instance, researchers have used in-situ neutron diffraction to study deformation induced twinning in HEAs [12–15] and in more

recent studies the transformation response of metastable HEAs [9,16,17]. During deformation, in-situ neutron diffraction probes the hkl-specific elastic-plastic response by monitoring the changes in each diffraction peak's position, broadening, and integrated intensity. By monitoring the intensities, strain-induced transformation can be evidenced. Fu et al. [16] demonstrated this using in-situ neutron diffraction, by evidencing the deformation-induced twinning in the hexagonal phase alongside about 80% transformation in the metastable $\text{Fe}_{50}\text{Mn}_{30}\text{Cr}_{10}\text{Co}_{10}$ alloy (DP-HEA). In a subsequent study, Liu et al. [9] used in-situ neutron diffraction to depict the effect of composition on the activation of TRIP. In their study, SFE values of four HEAs in the $\text{Fe}_{20}\text{Mn}_{20}\text{Cr}_{20}\text{Co}_y\text{Ni}_{40-y}$ system are systematically measured using TEM. As expected, they found that as metastability increased the density of stacking faults increased. They further noted that the measurement for the most metastable alloy was difficult due to the high density of stacking faults and dislocations. Thus, in-situ neutron diffraction may be an ideal approach to simultaneously measure SFE and probe the deformation-induced twinning and transformation behavior of a highly metastable HEA.

Understanding metastability in HEAs is important to obtaining a high strength-ductility combination. Obviously, the decrease in γ -f.c.c. phase stability results in an increase in ϵ -h.c.p. phase stability, and stabilization of a higher initial ϵ -h.c.p. phase fraction will be more thermodynamically favorable. Li et al. [18] confirmed that in the $\text{Fe}_{50}\text{Mn}_{30}\text{Cr}_{10}\text{Co}_{10}$ alloy (DP-HEA) with similar grain size, the increase in fraction of ϵ -h.c.p. prior to deformation was related to the simultaneous enhancement of strength and ductility. The relationship between the ϵ -h.c.p. fraction prior to deformation and the mechanical response provided motivation for two important directions of study in these alloys: Establishment of an understanding of (1) the effect of

metastability on the deformation mechanisms active during deformation; and (2) compositional design to achieve higher ϵ -h.c.p. phase stability (i.e., increased metastability).

Accordingly, many ensuing studies have probed both the structure and deformation response of the ϵ -h.c.p. phase [2,4,19]. For instance, Wei et al. [20] and Bu et al. [21] reported axial ratios of $\sim 1.616 \text{ \AA}$ and $\sim 1.624 \text{ \AA}$ in DP-HEA, similar to Mg alloys. Understanding the structure of the alloy increases the feasibility that similar deformation mechanisms, such as deformation twinning and pyramidal $\langle c+a \rangle$, slip would accommodate strain at higher stresses. In line with this idea, Nene et al. [2] postulated that activation of pyramidal $\langle c+a \rangle$ slip was likely responsible for ductility observed in the ϵ -h.c.p. phase, which was later evidenced along with significant $\langle a \rangle$ slip in DP-HEA [21].

Regarding the aim for achieving higher metastability, the subsequent design efforts were exactly opposite. Alloy design efforts instead have been aimed at stabilization of γ -f.c.c. in order to activate TRIP alongside strain induced twinning (TWIP) by increasing SFE. For instance, Li et al. [22] studied the effect of Mn, C and Ni on SFE and the corresponding deformation response. The addition of these elements increased the free energy difference between the γ -f.c.c. and ϵ -h.c.p. phases ($\Delta G^{\gamma \rightarrow \epsilon}$), increasing SFE and decreasing the initial ϵ -h.c.p. fraction. On the other hand, Nene et al. [1] confirmed that adding Si to the FeMnCrCo system increased the ϵ -h.c.p. phase fraction and, Sinha et al. [23] showed that substituting Co content at the expense of Ni in the $\text{Fe}_{42}\text{Mn}_{28}\text{Cr}_{15}\text{X}_{10}\text{Si}_5$ (in at. %, where X=Co, Ni) system led to the activation of TRIP. Further supporting the significance of Co, Liu et al. [9] pointed out that increasing Co at the expense of Ni resulted in activation of TRIP in the equiatomic FeMnCrCoNi system by decreasing the SFE. Even still, the demonstrated benefit of enhanced mechanical properties by increasing the ϵ -h.c.p. fraction has received relatively little attention. Specifically, efforts to develop alloys that are more

metastable than DP-HEA have neither been given much attention nor been correlated with a measured difference in SFE.

Relating deformation response to composition-dependent metastability is important for understanding and predicting the deformation behavior of metastable HEAs. Thus, this research aims to obtain an understanding of enhanced metastability and the related micro-mechanisms active in the $\text{Fe}_{40}\text{Mn}_{20}\text{Cr}_{15}\text{Co}_{20}\text{Si}_5$ (in at. %) HEA. Due to the high penetration depth and spatial resolution inherent to neutron diffraction, in-situ neutron diffraction is used to investigate deformation behavior of both phases and experimentally determine the SFE of highly metastable $\text{Fe}_{40}\text{Mn}_{20}\text{Cr}_{15}\text{Co}_{20}\text{Si}_5$. Here focus is given to understanding the deformation activity in the ϵ -h.c.p. phase, to relate enhanced metastability of the f.c.c. phase of the low SFE HEA.

2. Experimental procedures and analysis

2.1. Alloy selection, processing and microstructural characterization

To benchmark the extent of metastability, Thermo-Calc software (TCFE9 database) was used to predict $\Delta G^{Y \rightarrow \epsilon}$ for a number of HEA, including CS-HEAs. For experimentally probing the alloy, CS-HEA was cast in a vacuum induction furnace with pure metals to achieve the nominal compositions. The cast plate of $300 \times 100 \times 6$ mm was subjected to microstructural refinement using friction stir processing (FSP). Although additional details on thermomechanical treatment can be found elsewhere [2], an important point to note is that tool rotational speed of 350 rotations per minute (RPM) was used. Normal direction (ND), processing direction (PD) and transverse direction (TD) are defined in the thermomechanical treatment schematic (Fig. 4 (a)), where microscopy was carried out in the ND within the processed region. Electron backscatter diffraction (EBSD) was carried out on a FEI Nova NanoSEM 230 scanning electron microscope with Hikari

Super EBSD detector, to evaluate microstructural evolution in the processed condition. A step-size of 0.075 μm was used for all scans on mini-tensile specimen as described in [2]. Analysis of EBSD data was carried out in TSL OIM software package.

2.2. Time-of-flight neutron diffraction experiments and analysis

Tensile specimens were extracted parallel to the processing direction (Fig. 3 (a)). Subsequently, the specimens were deformed on the VULCAN neutron diffractometer [ref] at the Spallation Neutron Source (SNS) at Oak Ridge National Laboratory. The first of two specimens was loaded until failure to evaluate plastic deformation behavior in the plastic regime, while a second specimen was deformed to a stress just above yielding stress, similar to previous studies [24,25]. A detailed description of the tensile loading procedures has been provided elsewhere [16]. The VULCAN beamline is designed for in-situ probing of deformation behavior in multiple directions during loading continuously. As a result, time-of-flight neutron diffraction patterns were simultaneously recorded in loading (LD, -90°) and transverse (TD, $+90^\circ$) directions during tensile deformation. The use of neutron diffraction is selected for the present study due to the penetration depth of neutron and resolution of high order peaks, critical for determination of SFE from a bulk specimen.

Following diffraction experiments, the General Structure Analysis System (GSAS) was used to analyze diffraction data using the Rietveld refinement method for calculating phase fractions. Following refinement, deformation-induced changes in the diffraction pattern were analyzed to understand the transformation kinetics and lattice reorientation behavior of CS-HEA. VDRIVE software [26] was used to analyze the TOF diffraction data for single peak fitting using a convolution of the back-to-back exponentials with the pseudo-Voigt function. Single peak fit data was used to evaluate hkl-specific changes in lattice strain evolution in CS-HEA. In-situ neutron

diffraction was used to correlate the macroscopic response to the micro-mechanical deformation behavior. During the experiment, the measured shift in the diffraction peak positions can be used to estimate the strain imposed on the crystal lattices in specific grains of families. The lattice strain for each grain family (ϵ_{hkl}) is given by Eq. 1, where unloaded lattice spacing and lattice spacing under an applied stress are d_0^{hkl} and d_i^{hkl} , respectively.

$$\epsilon_{hkl} = \frac{d_i^{hkl} - d_0^{hkl}}{d_0^{hkl}} \quad [1]$$

2.3. Measurement of stacking fault energy using in-situ neutron diffraction

Measurement of the SFE alloys using TEM and diffraction techniques have shown that TWIP occurs when SFE is between 15-30 mJ m⁻², while TRIP has been observed below 20 mJ m⁻² [27]. SFE also can be estimated by its dependency on the $\Delta G^{Y \rightarrow \epsilon}$. This estimation method is typically observed using modeling to estimate the $\Delta G^{Y \rightarrow \epsilon}$. For example, Li et al. [22] used Thermo-Calc TCFE7 database predictions of $\Delta G^{Y \rightarrow \epsilon}$ to show that Mn and Ni additions in metastable HEAs suppress both the thermal and athermal martensite and also increase SFE. In the present study we used Thermo-Calc TCFE9 database to predict the effect of Si on $\Delta G^{Y \rightarrow \epsilon}$. The corresponding SFE is predicted by the relationship given in Eq. 2, where n , ρ and $\sigma^{Y/\epsilon}$ represent the number of planes, the planar density and the interfacial energy between the two phases, respectively.

$$\text{SFE} = n\rho\Delta G^{Y \rightarrow \epsilon} + n\sigma^{Y/\epsilon} \quad [2]$$

In addition to predictions using $\Delta G^{Y \rightarrow \epsilon}$ and measurement of partial separation width using TEM, SFE is measured experimentally by the relationship with stacking fault probability (P_{sf}) [28]. The P_{sf} is estimated by measuring the shift diffraction peak, i.e., the change in lattice strain (ϵ_{hkl}), between two crystallographically equivalent planes. In the present study, the {111} and the higher

order {222} families of grains were used. The relationship between P_{sf} and lattice strain is given by Eq. 3:

$$\varepsilon_{\{222\}} - \varepsilon_{\{111\}} = -\frac{\sqrt{3} \sum_b(\pm L_0)}{4\pi h_0^2(u+b)} P_{sf} \quad [3]$$

The term $\frac{\sum_b(\pm L_0)}{h_0^2(u+b)}$ is determined by crystallographic orientations selected as detailed in [24,25,28]

The {111} and {222} orientations are reported to have values of +1/4 and -1/8, respectively, giving rise to the following simplified expression relating lattice strain and P_{sf} . (Eq. 4).

$$P_{sf} = \frac{1}{0.0517} (\varepsilon_{\{222\}} - \varepsilon_{\{111\}}) \quad [4]$$

The relationship between SFE and P_{sf} is given by Eq. 5 [24,25], where a_0 and ε_{50}^2 are the lattice parameters for the γ -f.c.c. phase and mean square strain, respectively. The method for determination of ε_{50}^2 can be found in [11,29].

$$SFE = \frac{6.6a_0}{\pi\sqrt{3}} \left(\frac{2c_{44}}{c_{11} - c_{12}} \right)^{-0.37} \frac{\varepsilon_{50}^2}{P_{sf}} \left(\frac{c_{44} + c_{11} - c_{12}}{3} \right) \quad [5]$$

In Eq. 5, c_{11} , c_{12} and c_{44} are the three single crystal elastic constants (SCECs). In polycrystalline materials, the deformation response for each family of grains is different due to the anisotropic behavior of crystals. One way of evaluating the response is to measure elastic constants using in-situ neutron diffraction [14,30–34]. For cubic materials, by measuring lattice strain in both the LD and TD directions, both the hkl-specific Young's modulus (E_{hkl}) and Poisson's ratio (ν_{hkl}) diffraction elastic constants (DECs) can be obtained. Reciprocal diffraction elastic constants obtained from in-situ neutron diffraction experiments are used to minimize the cost function (Eq. 6) in order to determine the SCECs. By simultaneously solving the cost function with the Kroner's self-consistent model using the SCECs as free-fitting parameters their values can be determined,

as detailed by Wang et al. [30]. In the cost function, n and e represent the number of families of grains and experimental errors, respectively. For further detail, the reader is referred to [12,14,30,32,34].

$$\chi^2 = \sum_{i=1}^n \frac{\left(\left(\frac{1}{E_{hkl}} \right)_{\text{exp},i} - \left(\frac{1}{E_{hkl}} \right)_{\text{mod},i} \right)^2}{e_{1,i}^2} + \frac{\left(\left(\frac{v_{hkl}}{E_{hkl}} \right)_{\text{exp},i} - \left(\frac{v_{hkl}}{E_{hkl}} \right)_{\text{mod},i} \right)^2}{e_{2,i}^2} \quad [6]$$

3. Results and discussion

3.1. Measurement of stacking fault energy

Figure 1 (a) shows the observed diffraction patterns in the LD corresponding to the applied macroscopic stress of 0 MPa, 300 MPa, and 800 MPa. Good resolution of both the {111} and the higher order {222} families of grains can be observed throughout deformation. Further, the peak shifts for both families of grains are presented in Figs. 1 (b) and 1 (c). With increasing applied stress, the peak shift, i.e., change in lattice spacing, is tracked to measure the P_{sf} . As the applied stress increases, {111} and {222} intensities decrease and are accompanied by peak shifts, an increase in lattice spacing, d_{hkl} . Using Eq. 4, the P_{sf} of CS-HEA is determined to be 0.046 as compared to a maximum of ~0.02 and for TWIP HEAs in the literature [11]. Importantly, the higher the P_{sf} , the larger the area of the stacking fault and the lower the SFE [35].

Figure 1 (d) shows the DEC's measured from in-situ neutron diffraction, $1/E_{hkl}$ and v_{hkl}/E_{hkl} , plotted with results from simultaneous minimization using Kroner's self-consistent model. Here the data points represent experimental DEC's, tabulated below in Table 1; while the model results are shown by the black and red curves. Following minimization, the SCECs were $c_{11} = 174.2$ GPa, $c_{12} = 97.9$ GPa, and $c_{44} = 139.7$ GPa, comparable to values reported in the literature for Fe-based shape

memory alloys [36]. Thus, the determined SFE of CS-HEA is 5.24 mJ m^{-2} . Table 1 and Table 2 below present the measured DECs and a comparison of the determined SCECs to literature values for FeMnSi shape memory alloys, respectively.

Table 1. Diffraction elastic constants (DECs) of the γ -f.c.c. phase in CS-HEA

Family of grains	{200}	{311}	{420}	{220}	{422}	{111}
A_{hkl}	0	0.157	0.157	0.25	0.25	0.33
$1/E_{hkl} \text{ (TPa}^{-1}\text{)}$	7.19	5.04	5.15	3.87	4.12	4.21
$\nu_{hkl}/E_{hkl} \text{ (TPa}^{-1}\text{)}$	2.05	1.66	0.737	1.38	0.590	-1.05

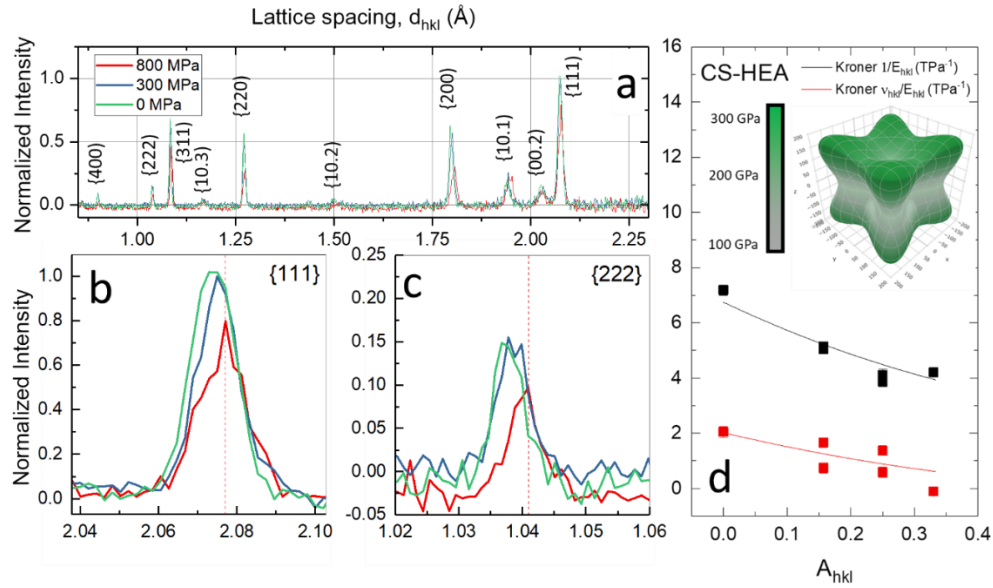


Figure 1. (a) Observed time of flight (TOF) neutron diffraction patterns at multiple stages of deformation and highlights of the peak shift for the (b) {111} and (c) {222} grain families. (d) Results from minimization of the reciprocal diffraction elastic constants (DECs) obtained from neutron diffraction; comparing experimental measurements (data points) with the Kroner's Self-Consistent model (lines). The inset in (d) provides a visualization of the anisotropy of the elastic modulus [37].

Table 2. Comparison of single crystal elastic constants (SCECs) for CS-HEA to FeMnSi alloys

Alloy (at. % Si)	Fe/Mn Si ₀		Fe/Mn Si ₂		Fe/Mn Si ₄		Fe/Mn Si ₆		Fe/Mn Si ₈		Fe ₄₀ Mn ₂₀ Cr ₁₅ Co ₂₀ Si ₅ (CS-HEA) Present study
C ₁₁ (GPa)	168 ^a	184 ^b	163 ^a	173 ^b	160 ^a	169 ^b	161 ^a	172 ^b	162 ^a	177 ^b	174
C ₁₂ (GPa)	110 ^a	125 ^b	107 ^a	117 ^b	105 ^a	115 ^b	109 ^a	120 ^b	112 ^a	127 ^b	98
C ₄₄ (GPa)	136 ^a	136 ^b	136 ^a	137 ^b	137 ^a	133 ^b	135 ^a	134 ^b	133 ^a	133 ^b	140

^a Fe:Mn ratio – 4.00 [36]

^b Fe:Mn ratio – 2.33 [36]

3.2. Relating enhanced metastability with stacking fault energy: Comparison of predicted and measured values

Based on literature observations, the addition of constituent elements such as Si and Co is expected to increase metastability, i.e., decreasing $\Delta G^{\gamma \rightarrow \epsilon}$, in agreement with Figs. 1 (a) and 1 (b), respectively. Considering the importance for SFE to the deformation response of γ -f.c.c. metals, also important to note is that the decrease of $\Delta G^{\gamma \rightarrow \epsilon}$ results in a decrease in SFE in the γ -f.c.c. phase (Eq. 2). In line with the relation between SFE and deformation behavior, single-phase γ -f.c.c. alloys have a higher $\Delta G^{\gamma \rightarrow \epsilon}$ than alloys exhibiting TRIP; thus, the green-filled symbols indicate alloys that have exhibited the strain-induced transformation experimentally. To further understand the effect of metastability on deformation response, the schematic presented in Fig. 2 shows a decrease in both $\Delta G^{\gamma \rightarrow \epsilon} / \text{SFE}$ (the ordinate axes) corresponding to the increase in both the density of stacking faults, i.e., P_{sf} , in the γ -f.c.c. phase. Again, the higher the P_{sf} the lower the SFE [35]. The increase of Si or Co increases the density of stacking faults in the γ -f.c.c. phase, and results in more potential nucleation sites for the ϵ -h.c.p. phase. Increasing the sites for nucleation of ϵ -h.c.p. is expected to be responsible for increases in the ϵ -h.c.p. phase dominance, i.e., ϵ -h.c.p. fraction greater than 50% prior to deformation.

The $\Delta G^{Y \rightarrow \epsilon}$ [22] and SFE [38] have been reported for metastable HEAs using Thermo-Calc software (TCFE7) and were in good agreement with experimental observations. Here we adopt the same approach to predict the change in $\Delta G^{Y \rightarrow \epsilon}$ for Si-containing metastable HEA systems. The first system, $\text{Fe}_{55-x}\text{Mn}_{30}\text{Cr}_{10}\text{Co}_{10}\text{Si}_x$ (indicated by the dashed line), includes Si in the well-known DP-HEA as a reference of metastability and well-studied deformation response (Fig. 2 (a)). With the addition of Si, $\Delta G^{Y \rightarrow \epsilon}$ decreases to less than -1000 J mol^{-1} . Similarly, the $\text{Fe}_{45-x}\text{Mn}_{20}\text{Cr}_{15}\text{Co}_{20}\text{Si}_x$ system investigated in the present study (indicated by solid line) is predicted to decrease from $\sim 200 \text{ J mol}^{-1}$ to less than -8000 J mol^{-1} with the addition of Si up to $\sim 7 \%$. In addition, Figure 2 (b) shows the effect of Co as evidenced by Liu et al. [9]. Figure 2 (b) serves as a comparison of the present study to alloys ranging in Co: Ni ratio from 1:1 to 3:1; i.e., from the equiatomic FeMnCrCoNi to $\text{Fe}_{20}\text{Mn}_{20}\text{Cr}_{20}\text{Co}_{30}\text{Ni}_{10}$ by exchanging Co for Ni. They showed a transition in deformation mechanisms occurred by decreasing $\Delta G^{Y \rightarrow \epsilon}$ below $\sim 750 \text{ J mol}^{-1}$ in opposition to twinning and slip above this value [39]. They confirmed that the most metastable alloy exhibited TRIP, and thus led to the highest strength-ductility combination. Figures 2 (a) and 2 (b) provide a relative comparison of metastability of alloys in the literature to the present alloy and highlight the enhanced metastability expected by prediction.

The predictions of $\text{Fe}_{40}\text{Mn}_{20}\text{Cr}_{15}\text{Co}_{20}\text{Si}_5$ (solid line at $X = 5 \text{ at. \% Si}$) (Fig. 2 (a)) are compared with the experimental SFE measurement from the present study. The difference between predicted and experimental ($\sim 29 \text{ mJ m}^{-2}$) is substantial and suggests that one should be careful in predicting values of SFE using Thermo-Calc and that experimental verification is necessary. Nevertheless, the database seems suitable for relative comparison, as the predictions agree with prior studies by the present authors on both DP-HEA [40] and CS-HEA [2]. Specifically, considering CS-HEA is

predicted to be more metastable than DP-HEA, as expected, it exhibits a significantly larger fraction of ϵ -h.c.p.

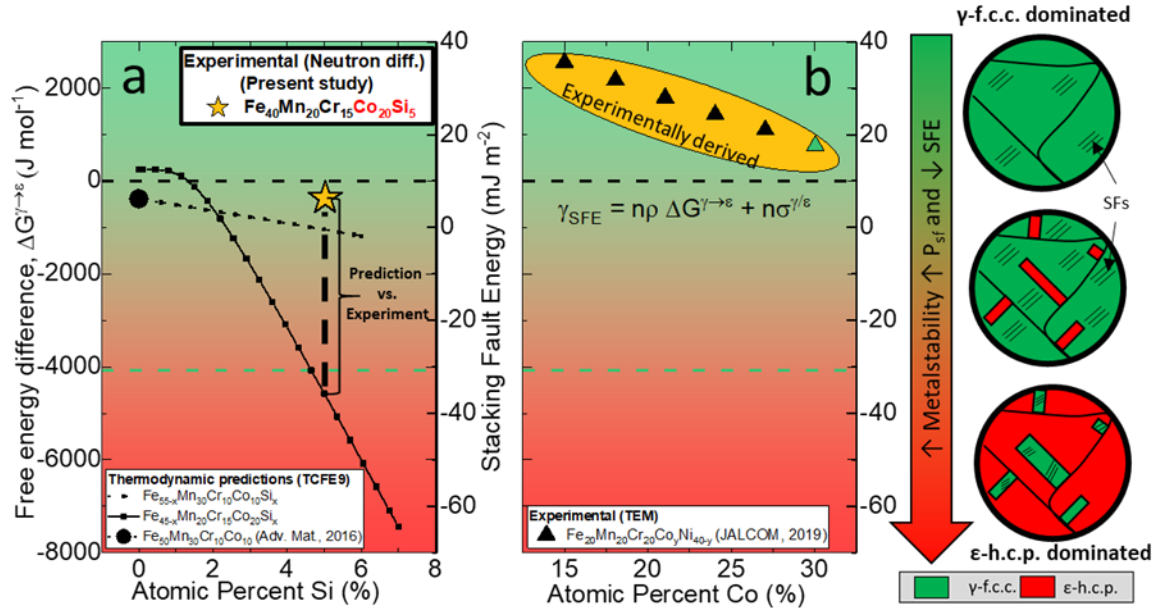


Figure 2. Designing for metastability: The effect of Si and Co on the free energy difference between phases ($\Delta G^{\gamma \rightarrow \epsilon}$) and stacking fault energy (SFE). (a) The effect of adding Si in the $\text{Fe}_{55-x}\text{Mn}_{30}\text{Cr}_{10}\text{Co}_{10}\text{Si}_x$ and $\text{Fe}_{45-x}\text{Mn}_{20}\text{Cr}_{20}\text{Co}_{20}\text{Si}_x$ system (b) The effect of Co determined experimentally in the $\text{Fe}_{20}\text{Mn}_{20}\text{Cr}_{20}\text{Co}_y\text{Ni}_{40-y}$ system [9]. The green-filled symbols indicate alloys that have experimentally exhibited the strain-induced transformation from γ -f.c.c. \rightarrow ϵ -h.c.p.

3.3. Microstructural evolution and macroscopic tensile response

A schematic illustrating the in-situ neutron diffraction experimental setup used to probe the γ -f.c.c. \rightarrow ϵ -h.c.p. transformation behavior is shown in Fig. 3 (a). Here the green line indicates the incident neutron beam, while the two detectors labeled D_1 and D_2 correspond to the LD and TD, respectively. The tensile loading direction is indicated by the translucent arrows, while the

scattering vectors, $\vec{Q}_{LD\parallel}$ and $\vec{Q}_{TD\perp}$, are represented by the two orange arrows. Important to understanding deformation behavior, strain accommodation and lattice reorientation for specific grain families are evaluated using measurements from both the LD and TD. Both γ -f.c.c. and ϵ -h.c.p. grain families with their hkl-plane normals oriented parallel to their scattering vectors, either $\vec{Q}_{LD\parallel}$ and $\vec{Q}_{TD\perp}$, are observed in the LD and TD detectors [41]. Thus, neutron diffraction establishes a means to carefully probe the kinetics of both transformation and lattice reorientation-related twinning events during deformation.

Phase and texture evolution resulting from FSP is related to the deformation response of CS-HEA, specifically texture evolution in the ϵ -h.c.p. phase. The phase fraction of γ -f.c.c. and ϵ -h.c.p. phases prior to tensile straining have an effect on phase evolution during deformation [16,18]. CS-HEA is predominantly of the ϵ -h.c.p. phase confirmed by quantitative phase analysis (QPA) of the neutron diffraction patterns in both the LD and TD directions, Figs. 3 (b) and 3 (c) respectively. Comparing the diffraction patterns makes apparent that both directions have similar measured phase fractions; an example of the opposing case is presented in [42]. Phase fractions before deformation were determined to be 42% γ -f.c.c. and 58% ϵ -h.c.p. Phase evolution resulting from FSP was attributed to the combination of strain rate and temperature, which led to the initially ϵ -h.c.p. dominated microstructure [2,43]. In addition to the initial phase fractions, some insight on texture can also be obtained by comparing {00.2}, {10.1}, {10.2} and {10.3} peaks. The comparable LD and TD diffraction patterns also suggest no significant direction-dependent texture in the bulk measurement of the specimen is observed following FSP.

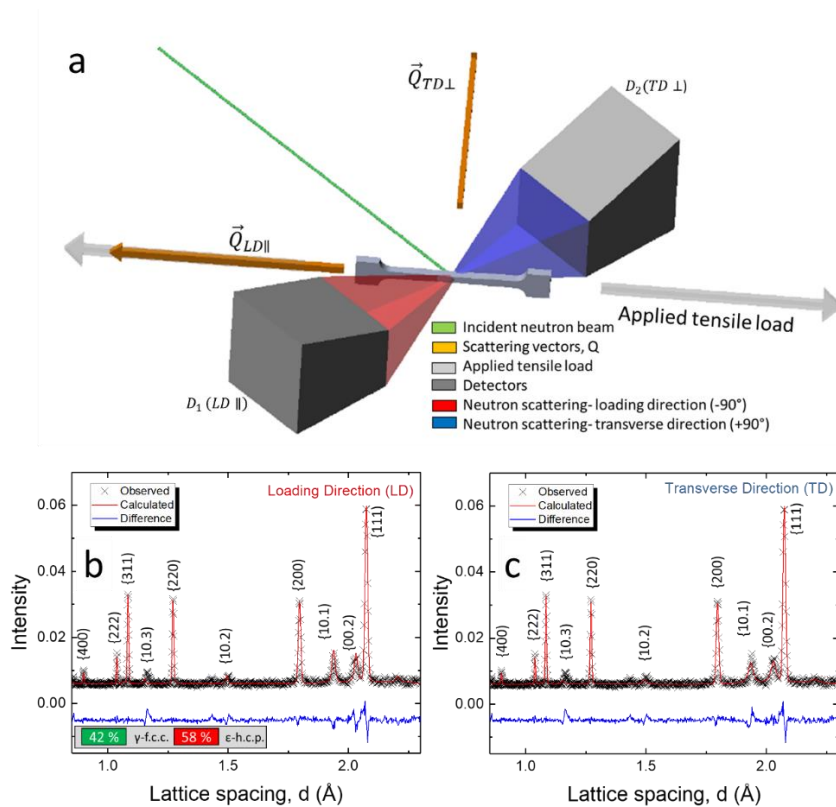


Figure 3. A schematic of the (a) time-of-flight (TOF) neutron diffraction experimental setup and neutron diffraction patterns for CS-HEA in both the (b) loading (LD) and (c) transverse directions prior to deformation.

Grain orientation is important in processing of ϵ -h.c.p. metals in that basal slip does not satisfy von Mises's criterion, and thus requires five independent slip systems. Accordingly, the deformation response of ϵ -h.c.p. structured metals and alloys depends heavily on their texture evolution. While neutron diffraction results suggested no significant texture, EBSD was carried out normal to the surface of the process region for a more localized evaluation (Figs. 3 (a) and 3 (b)). Figures 4 (b₁), 4 (b₂) and 4 (c) show the inverse pole figure (IPF) map, phase map and basal pole figure (PF), respectively. The IPF map and basal PF further suggest that the martensite grains are randomly

oriented, with an average grain size $\sim 6 \mu\text{m}$. Additionally, local evaluation using EBSD reveals similar intensities in the PF, further supporting the absence of any preferred orientation.

The work hardening response and deformation mechanisms in fine-grained CS-HEA are probed during tensile deformation. The macroscopic stress-strain response confirms that, before fracture, the specimen reaches a peak stress of $\sim 1400 \text{ MPa}$ and exhibits good work hardenability following macroscopic yielding at $\sim 650 \text{ MPa}$ (Fig. 4 (d)). During deformation, the γ -f.c.c. phase fraction decreases due to the onset of TRIP. Figure 4 (e) shows the initial γ -f.c.c. phase fraction of 42% begins to decrease at $\sim 700 \text{ MPa}$ in CS-HEA. Importantly, in comparison to a recent neutron diffraction study on DP-HEA [16], CS-HEA exhibits a marginal fraction of transformation with increasing applied stress (Fig. 4 (e)). The lower transformed fraction insists that the work hardening response may be attributed to mechanisms other than transformation. DP-HEA exhibits a transformed fraction of about 60%, as compared to the $\sim 25\%$ in CS-HEA in the present study, although worth mentioning is the difference in grain size, considering DP-HEA studied by neutron diffraction was $\sim 45 \mu\text{m}$ [16]. Grain size is expected to have some effect on transformation behavior, although the relationship between the effect of grain size and initial ϵ -h.c.p. fraction on work hardening has been complex to separate [18]. Considering our previous work on DP-HEA ($\sim 6.5 \mu\text{m}$) and CS-HEA ($\sim 6 \mu\text{m}$), both alloys had similar grain sizes after undergoing identical processing conditions as in the present study. The DP-HEA with $45 \mu\text{m}$ and $6.5 \mu\text{m}$ grain sizes both exhibited transformed fractions of 60% and 69%, respectively, suggesting that significant stabilization of the γ -f.c.c. phase and TRIP occurs irrespective of grain size in this alloy. These results imply that the difference in work hardenability is likely due to CS-HEA's high initial fraction of ϵ -h.c.p., thus demonstrating the benefit of engineered metastability aside from grain size.

In line with understanding the effect of metastability on work hardening, the ϵ -h.c.p. phase fraction prior to deformation is likely to have modified the stress partitioning behavior of the alloy. Figure 4 (d) shows the estimated stresses for γ -f.c.c. and ϵ -h.c.p. phases and makes apparent that during plastic deformation, the ϵ -h.c.p. phase accommodates significantly larger stress than the γ -f.c.c. phase. The effect of metastability on stress partitioning can be understood by Eq. 7. The phase stresses can be determined by Hooke's law, where the stress of each phase is dependent on the modulus and lattice strain, where similar lattice strain evolution of the two phases is observed in CS-HEA. Considering both phases have similar moduli (E_i) [4,16] and the observance of similar lattice strain (ϵ_i) evolution of phases in CS-HEA, stress partitioning behavior is likely to be dependent on the initial phase fractions (f_i) given by Eq. 7 [16,44].

Further, considering the large stress partitioned to the ϵ -h.c.p. phase, likely deformation twinning and pyramidal $\langle c+a \rangle$ slip have occurred during deformation. In support of deformation twinning, Figs. 4 (f) and 4 (g) show that grain elongation of the ϵ -h.c.p. phase along with changes in texture have occurred following deformation, thus indicating significant deformation accommodation in the ϵ -h.c.p. phase. A combination of $\{10.3\}$ twins and $\{10.2\}$ twins are revealed by EBSD (Figs. 3 (f₁)–3 (f₃)), with measured misorientations for $\{10.3\}$ twins shown later in Fig 6 (c₂). Twinning for the $\{10.1\}$ and $\{10.3\}$ families of grains is characterized by misorientations of 56.2° and 64° , respectively. The misorientation of 86.2° for the $\{10.2\}$ extension twins (Fig. 4 (f₃)) is highlighted within the IPF map. To further confirm the occurrence of twinning during deformation, further analysis was carried out on single peak fit data acquired by in-situ diffraction experiments.

$$\sigma = f_{f.c.c.} (E_{f.c.c.} \epsilon_{\{200\}}) + f_{h.c.p.} (E_{h.c.p.} \epsilon_{\{10.1\}}) \quad [7]$$

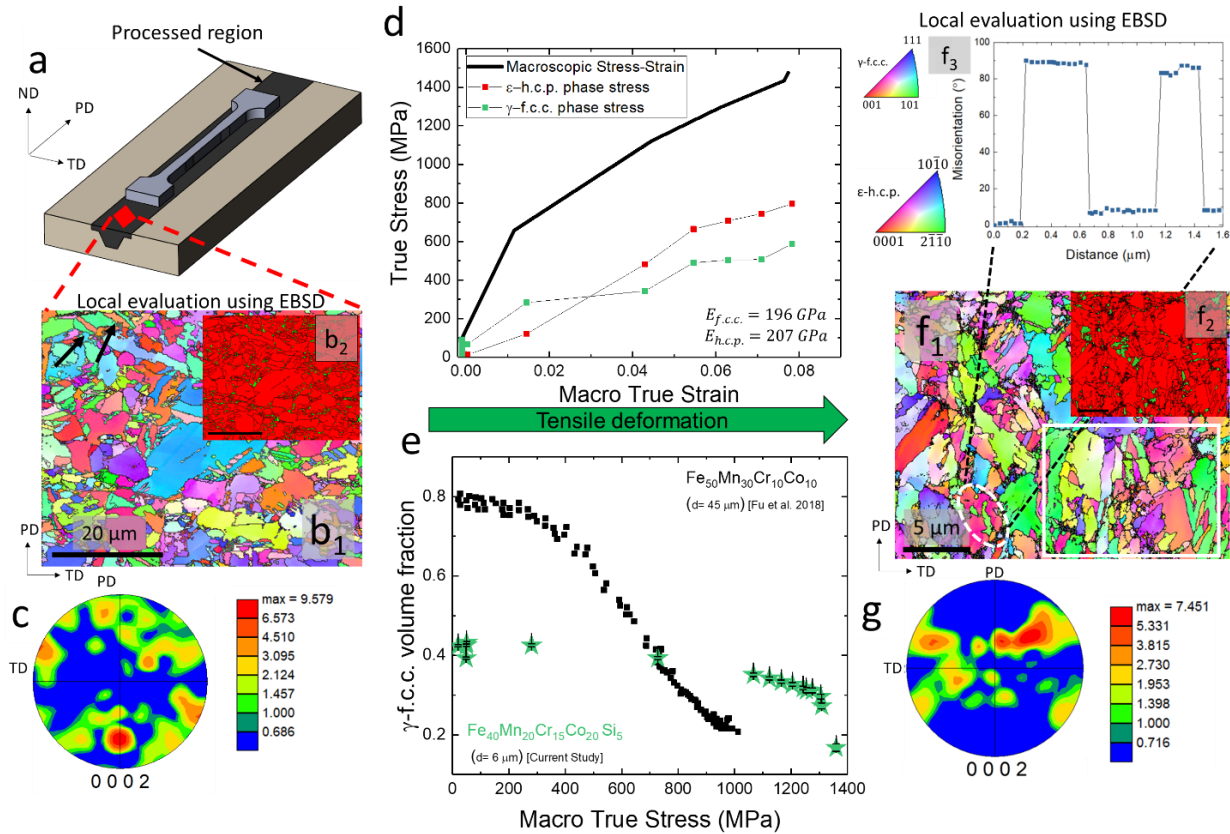


Figure 4. Macroscopic stress-strain response and transformation behavior of CS-HEA captured by neutron diffraction. (a) Schematic representation of specimen extraction location. (d) Macroscopic true stress-strain response and (e) comparison of the transformation behavior of CS-HEA to DP-HEA [16] captured using in-situ neutron diffraction. Local evaluation of CS-HEA phase fractions prior to deformation shown by electron backscatter diffraction (b₁) inverse pole figure map, (b₂) phase map, and (c) pole figure while the same is shown for deformed condition in (f₁), (f₂) and (g), respectively. (f₃) Shows measured misorientation of $\sim 86.2^\circ$ revealing twins in the ϵ -h.c.p. phase following deformation.

3.3.1. The effect of metastability on the micromechanical behavior of ϵ -h.c.p.

3.3.1.1. Deformation twinning and Pyramidal $\langle c+a \rangle$ slip

As the larger initial phase fraction is expected to have increased stress partitioning to the ϵ -h.c.p. phase, understanding the mechanisms that lead to large ductility in ϵ -h.c.p. dominated CS-HEA is important [2]. The current section discusses the micro-mechanisms activated using in-situ neutron diffraction results. Figures 5 (a) and 5 (b) show the lattice strain evolution of the $\{10.1\}$, $\{10.2\}$, $\{10.3\}$, and $\{00.2\}$ families of grains with increasing applied stress. For each family of grains, the LD (half-filled) and the TD (filled) are shown; negative or positive values indicate compressive and tensile strain accommodation, respectively. As expected, the TD direction exhibits a negative lattice strain, and the LD exhibits a positive lattice strain for the $\{10.1\}$, $\{10.2\}$ and $\{10.3\}$ grains due to the Poisson effect. Interestingly, the $\{00.2\}$ family of grains exhibits an anisotropic response under loading. Compressive strain accommodation is observed in the TD, while no significant change in lattice strain evolution exhibited in the LD suggests that in the LD, the activity of non-basal slip systems dominates in strain accommodation [45]. The $\{00.2\}$ family of grains was observed to accommodate strain in the LD in a recent report [16] in a randomly textured DP-HEA. Thus, likely lack of strain accommodation in the LD for the $\{00.2\}$ is due to the initial texture and higher metastability of CS-HEA.

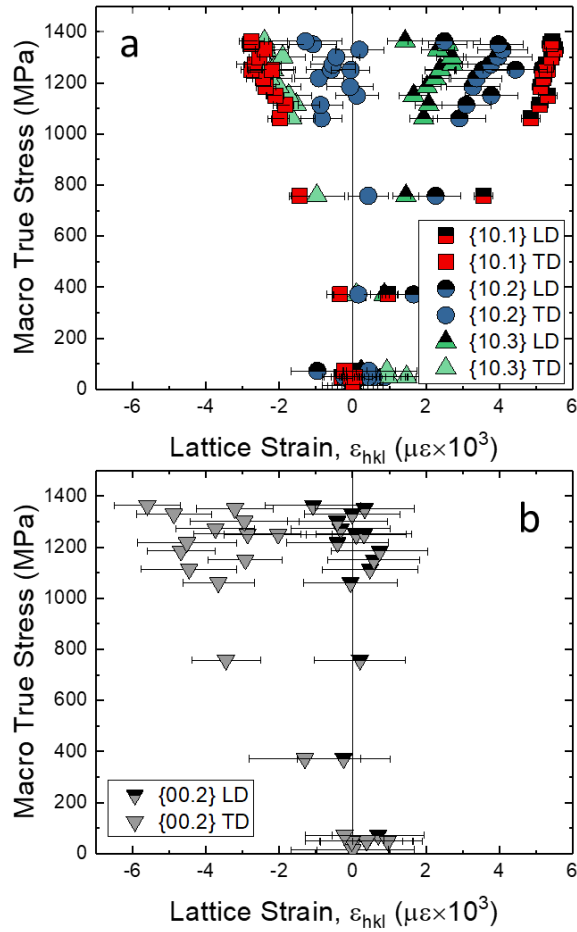


Figure 5. Lattice strain evolution with increasing applied stress measured in the loading (LD) and transverse (TD) directions for families of grains in the hexagonal phase.

In addition to lattice strain related to peak shift, the change in integrated intensity of diffraction peaks in various grain families can be used to understand changes in orientation and phase fraction. Without a change of chemistry, integrated intensity is proportional to the volume of families of grains that are aligned with a particular direction. Thus, by comparing intensity changes, lattice reorientations are captured using multiple detectors during neutron diffraction experiments [45–47]. Further, lattice reorientation is possible to evidence with multiple detectors due to the fact that each detector probes grain families with their plane normal-oriented parallel to the respective

detector's scattering vector [41], as shown schematically in Fig. 6 (c₁). In the present study, lattice reorientation can be observed in the {10.1}, {10.2} and {10.3} families of grains in the present CS-HEA (Figs. 6 (c)–6 (d)), as indicated by the divergence of the LD and TD intensities. Fu et al. [16] evidenced both {10.1} and {10.3} contraction twinning and {10.2} extension twinning in DP-HEA marked by the splitting of intensities in the LD and TD, related to significant lattice reorientations. Specifically, extension twinning in CS-HEA is indicated by the divergence of {00.2} intensities indicating the near 90° rotation of {10.2} grains from the TD to LD [16,45]. The {10.3} contraction twins are shown in the EBSD IPF map along with their measured misorientations, Figs. 6 (c₂) and 6 (c₃–c₄), respectively. Lattice reorientation occurring in the {10.3} grains is shown in Fig 6 (c) and schematically represented in Fig. 6 (c₁). The {10.3} family of grains exhibits an intensity increase and decrease in the TD and LD with increasing applied stress, respectively. This indicates significant reorientation and is confirmed by the observed deformation twins (Fig. 6 (c₂)). The multiple instances of twinning are likely to have led to the exceptional work hardening response owing to immense stress partitioning.

Contraction twinning of the {10.1} family of grains can be expected by the observed increase in LD of the {10.1}, while both {10.2} and {10.3} increase in the TD [16]. This lattice reorientation is shown in Figs. 6 (a)–6 (c), although the increases in the {10.2} and {10.3} intensities are marginal, and {10.1} contraction twins are not observed in the microstructure (Figs. 4 (f₁) and 4 (c₂)). Furthermore, the near equal intensities in the LD and TD of the grain families suggest the c-axes of some grains are initially oriented close to the tensile axis [16]. Importantly, the absence of {10.1} twins in the microstructure along with the low intensities of the {10.2} and {10.3} grains point to the idea that compression along the c-axis may not solely be a result of {10.1} deformation twinning in CS-HEA.

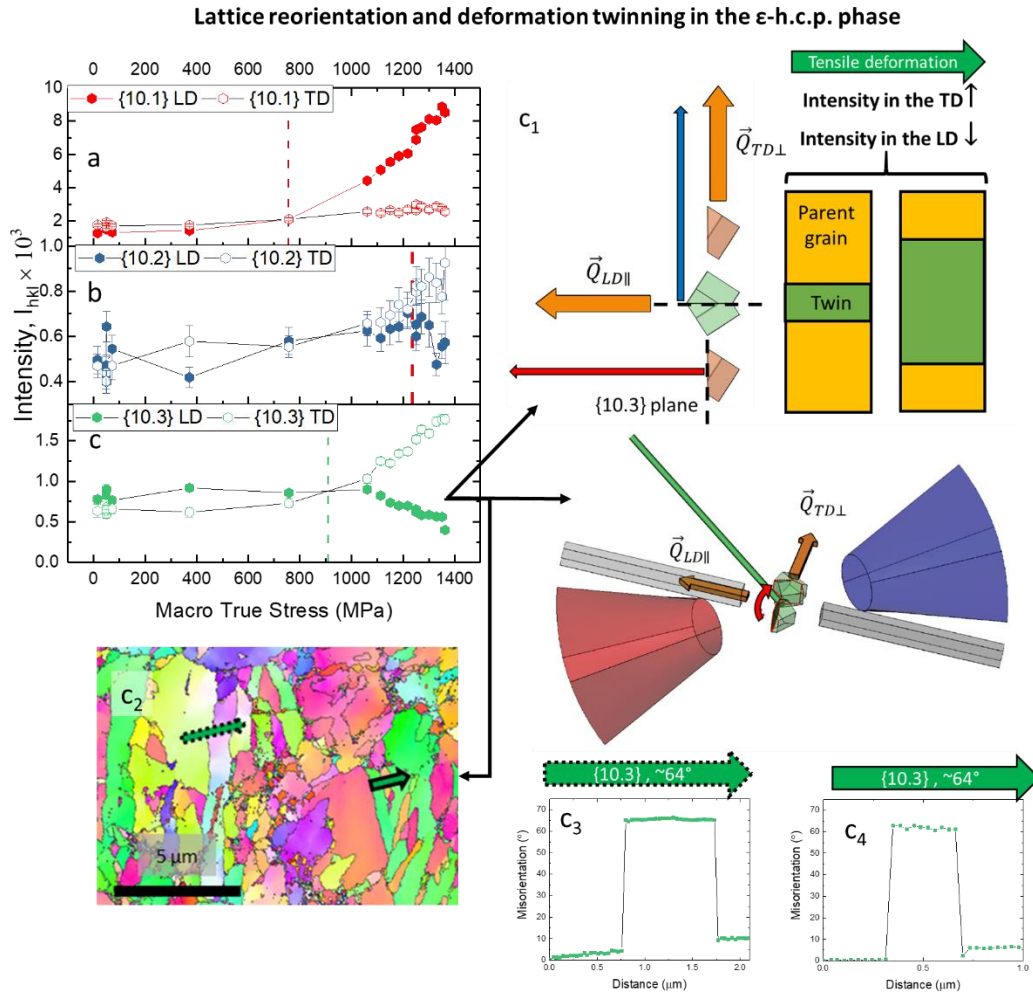


Figure 6. Micromechanical deformation response of the ϵ -h.c.p. phase. The intensity change with increasing applied stress measured in the loading and transverse directions for the (a) $\{10.1\}$ (b) $\{10.2\}$ and (c) $\{10.3\}$ families of grains. (c₁) Schematic representation of the lattice reorientation occurring with increasing stress and the increase of intensity in the transverse direction with $\{10.3\}$ twinning. (c₂) Inverse pole figure map showing $\{10.3\}$ deformation twins with measured misorientations of $\sim 64^\circ$ are shown in (c₃) and (c₄).

The deformation-induced peak shift corresponds to changes in lattice strain (Eq. 1 and Figs. 5 (a) and 5 (b)). In addition, peak shifts can be related to changes in the a_ϵ and c_ϵ lattice parameters as a

function of applied load. In the undeformed condition, the γ -f.c.c. lattice parameter of $a_\gamma = 3.590$ Å and the lattice parameters of the ϵ -h.c.p. phase of $a_\epsilon = 2.539$ Å and $c_\epsilon = 4.112$ Å are determined using neutron diffraction, and result in an axial ratio (c/a ratio) of 1.619. Figures 7 (a)–7 (c) show the evolution of both hexagonal lattice parameters and axial ratio with increasing applied stress. Pure metals such as Co, Mg and Ti are indicated to highlight the significant decrease with applied stress. An additional important note is the simultaneous increase of a_ϵ and decrease of c_ϵ lattice parameters (Figs. 7 (a) and 7 (b)) with increasing stress, suggesting $\langle a \rangle$ and possibly $\langle c+a \rangle$ dislocation slip are likely to have occurred at the later stages of deformation, as reported in the literature for metastable HEAs [21].

Considering the possibility of pyramidal $\langle c+a \rangle$ slip, in hexagonal metals, plastic slip along the c -axis on pyramidal planes can occur only by $\langle c+a \rangle$ dislocations [45,48]. The decrease of c_ϵ agrees with the lattice strain evolution of the $\{00.2\}$ grains in Fig. 5 (a), which together suggest compression of the c -axis occurs. Thus it is possible that in the late stages of deformation, above ~ 1250 MPa, $\langle c+a \rangle$ slip would have occurred along the c -axis in either the parent $\{10.1\}$ grains or the c -axis of $\{10.1\}$ contraction twins [49,50]. C -axis compression of $\{10.1\}$ twins has been reported to exhibit pyramidal $\langle c+a \rangle$ slip as opposed to basal slip owing to large differences in Schmidt factor [49,51]. Moreover, with a change in the axial ratio, the dominant deformation mode and strain-induced texture evolution of hexagonal metals has been observed to change at room temperature [52]. Considering the large decrease in axial ratio exhibited CS-HEA, likely pyramidal $\langle c+a \rangle$ slip observed in metastable HEAs would occur later in deformation, consistent with the dependence of Schmidt factor upon the axial ratio [53]. At ~ 1250 MPa, the axial ratio has reduced to 1.597 as opposed to 1.619, significantly closer to the axial ratio of Ti (1.587), which exhibits pyramidal $\langle c+a \rangle$ slip more frequently [48].

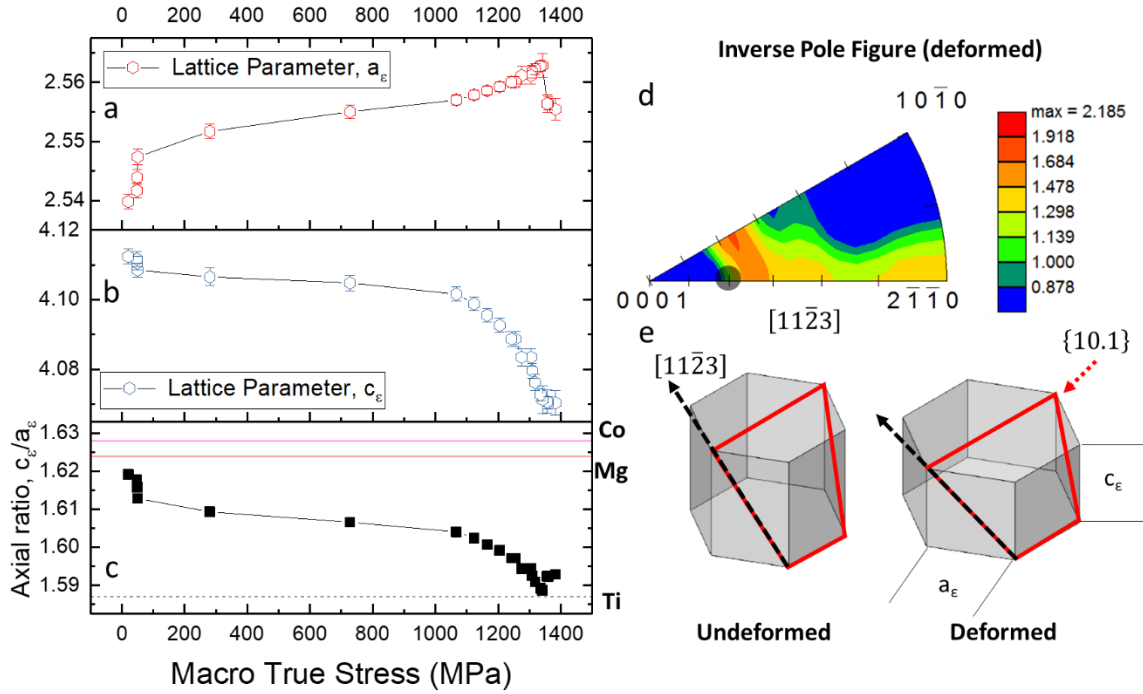


Figure 7. Evolution of ϵ -h.c.p. unit cell with increasing applied stress. Evolution of (a) Lattice parameter a_ϵ , (b) Lattice parameter c_ϵ and (c) axial ratio. Inverse pole figure of deformed CS-HEA showing intensity moderate intensity near the $[11\bar{2}3]$ direction corresponding to the $\{10.1\}\{11\bar{2}3\}$ first order pyramidal slip system along with a schematic showing change in the unit cell in undeformed and deformed states.

As discussed, SFE is closely related to deformation mode and thus has been observed to be related to work hardening behavior and strength [9,22]. Important to note is that experimental measurements of SFE for metastable HEAs are limited in the literature. This may be partially due to the difficulty in reliably measuring partial separation widths due to such high density of stacking faults and dislocations [9]. This difficulty discussed in microscopy demonstrates the strength of in-situ neutron diffraction for SFE measurement.

Figure 8 shows the relationship between experimental measurements of SFE with strength for metastable HEA studies and the present study (CS-HEA, 5.24 mJ m^{-2}). Here the SFE measurement from the present study is compared with measured SFE for the $\text{Fe}_{20}\text{Mn}_{20}\text{Cr}_{20}\text{Co}_y\text{Ni}_{40-y}$ system, which is of similar grain size. Transformation in metastable HEAs has been accepted to lead to enhanced work hardenability, although the present study shows that with a relatively marginal contribution of TRIP, a high strength-ductility combination can be achieved by non-basal strain accommodation in the hexagonal phase. The work hardenability and strength observed are due to the enhancement of metastability through compositional design, given similar grain sizes are compared. To emphasize the importance of this plot, the decrease of SFE demonstrates that strength can also be increased by further enhancement of metastability, as opposed to the traditional approach of strengthening of the γ -f.c.c. phase. Nevertheless, we maintain that this enhanced metastability promotes immense stress partitioning to the ϵ -h.c.p. phase during plastic straining, which then results in deformation twinning and potentially pyramidal $\langle c+a \rangle$ slip.

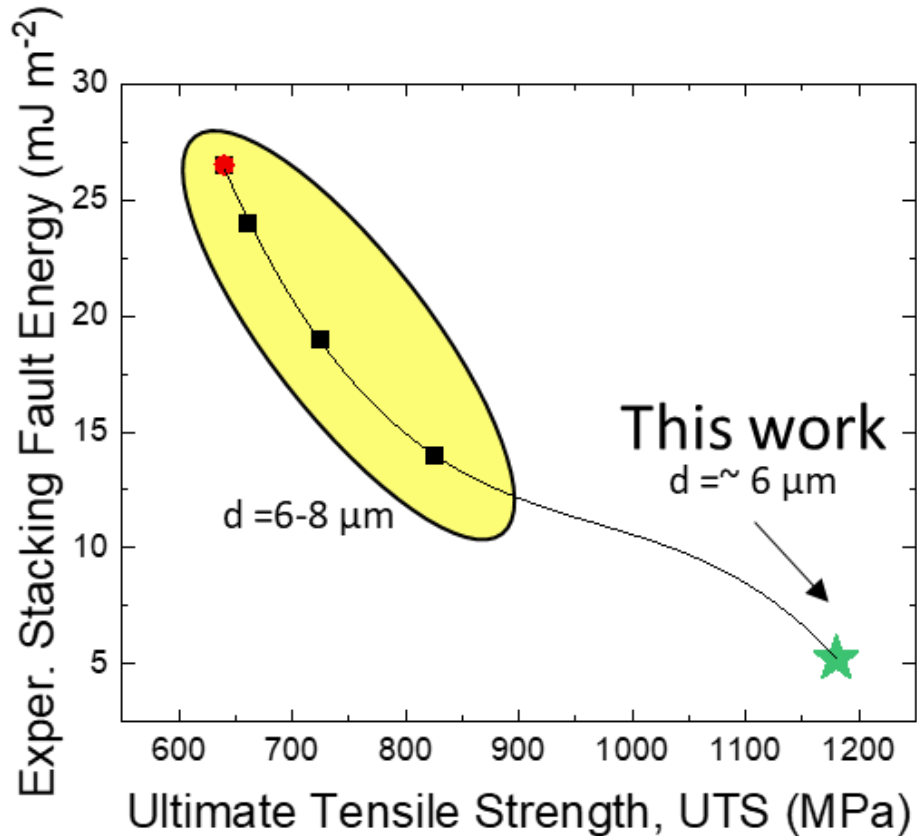


Figure 8. The relationship between strength and stacking fault energy for metastable HEA systems with similar reported grain size, showing that enhancement of metastability also leads to strength increases even with marginal transformation.

4. Conclusion

The present study demonstrates the effect of metastability on both deformation response and stacking fault energy (SFE) using in-situ neutron diffraction. Theoretical predictions are benchmarked with experimentally-determined SFE for $\text{Fe}_{40}\text{Mn}_{20}\text{Cr}_{15}\text{Co}_{20}\text{Si}_5$ (in at. %) CS-HEA (5.24 mJ m^{-2}). Increased metastability, i.e., lower $\Delta G^{\gamma \rightarrow \epsilon}$, stabilizes the ϵ -h.c.p. phase as opposed to γ -f.c.c., and results in a ϵ -h.c.p. dominant microstructure in the metastable CS-HEA. The initial ϵ -h.c.p. fraction governed the stress partitioning behavior between the γ -f.c.c. and ϵ -h.c.p. phases

during tensile deformation, resulting in a marginal fraction of transformation. Significant stress partitioning to the ϵ -h.c.p. phase results in marginal transformation, but instead, results confirm significant deformation twinning and lattice reorientation. In addition, changes in axial (c/a) ratio from 1.619 to 1.597 Å are likely accompanied by changes in Schmidt factor, leading to both twinning and pyramidal $\langle c+a \rangle$ in the later stages of deformation.

5. Additional Information

Acknowledgments: The present work was performed under a cooperative agreement between the Army Research Laboratory (ARL) and the University of North Texas (W911NF-19-2-0011). The authors thank the Materials Research Facility for providing access to the microscopy facilities at the University of North Texas.

Neutron diffraction work was carried out at the Spallation Neutron Source (SNS), which is the U.S. Department of Energy (DOE) user facility at the Oak Ridge National Laboratory, sponsored by the Scientific User Facilities Division, Office of Basic Energy Sciences. The authors thank Matthew Frost, Shivakant Shukla and Saket Thapliyal for their assistance in carrying out neutron diffraction experiments.

Competing interests: The authors declare no competing financial and non-financial interests.

References

- [1] S.S. Nene, M. Frank, K. Liu, R.S. Mishra, B.A. McWilliams, K.C. Cho, Extremely high strength and work hardening ability in a metastable high entropy alloy, *Scientific Reports*. 8 (2018) 9920. doi:10.1038/s41598-018-28383-0.
- [2] S.S. Nene, M. Frank, K. Liu, S. Sinha, R.S. Mishra, B. McWilliams, K.C. Cho, Reversed strength-ductility relationship in microstructurally flexible high entropy alloy, *Scripta Materialia*. 154 (2018) 163–167. doi:10.1016/j.scriptamat.2018.05.043.
- [3] S.S. Nene, S. Sinha, M. Frank, K. Liu, R.S. Mishra, B.A. McWilliams, K.C. Cho, Unexpected strength–ductility response in an annealed, metastable, high-entropy alloy, *Applied Materials Today*. 13 (2018) 198–206. doi:10.1016/j.apmt.2018.09.002.
- [4] S. Sinha, R.A. Mirshams, T. Wang, S.S. Nene, M. Frank, K. Liu, R.S. Mishra, Nanoindentation behavior of high entropy alloys with transformation-induced plasticity, *Scientific Reports*. (2019) 1–21. doi:10.1038/s41598-019-43174-x.
- [5] K. Liu, S.S. Nene, M. Frank, S. Sinha, R.S. Mishra, Extremely high fatigue resistance in an ultrafine grained high entropy alloy, *Applied Materials Today*. 15 (2019) 525–530. doi:10.1016/j.apmt.2019.04.001.
- [6] K. Liu, S.S. Nene, M. Frank, S. Sinha, R.S. Mishra, Metastability-assisted fatigue behavior in a friction stir processed dual-phase high entropy alloy, *Materials Research Letters*. 6 (2018) 613–619. doi:10.1080/21663831.2018.1523240.
- [7] S.S. Nene, M. Frank, K. Liu, S. Sinha, R.S. Mishra, B.A. McWilliams, K.C. Cho, Corrosion-resistant high entropy alloy with high strength and ductility, *Scripta Materialia*. 166 (2019) 168–172. doi:10.1016/j.scriptamat.2019.03.028.
- [8] S.F. Liu, Y. Wu, H.T. Wang, J.Y. He, J.B. Liu, C.X. Chen, X.J. Liu, H. Wang, Z.P. Lu, Stacking fault energy of face-centered-cubic high entropy alloys, *Intermetallics*. 93 (2018) 269–273. doi:10.1016/j.intermet.2017.10.004.
- [9] S.F. Liu, Y. Wu, H.T. Wang, W.T. Lin, Y.Y. Shang, J.B. Liu, K. An, X.J. Liu, H. Wang, Z.P. Lu, Transformation-reinforced high-entropy alloys with superior mechanical properties via tailoring stacking fault energy, *Journal of Alloys and Compounds*. (2019). doi:10.1016/j.jallcom.2019.04.035.
- [10] J. Liu, C. Chen, Y. Xu, S. Wu, G. Wang, H. Wang, Y. Fang, L. Meng, Deformation twinning behaviors of the low stacking fault energy high-entropy alloy: An in-situ TEM study, *Scripta Materialia*. (2017). doi:10.1016/j.scriptamat.2017.05.001.
- [11] B. Cai, B. Liu, S. Kabra, Y. Wang, K. Yan, P.D. Lee, Y. Liu, Deformation mechanisms of Mo alloyed FeCoCrNi high entropy alloy: In situ neutron diffraction, *Acta Materialia*. (2017). doi:10.1016/j.actamat.2017.01.034.
- [12] Y. Wu, W.H. Liu, X.L. Wang, D. Ma, A.D. Stoica, T.G. Nieh, Z.B. He, Z.P. Lu, In-situ neutron diffraction study of deformation behavior of a multi-component high-entropy alloy, *Applied Physics Letters*. 104 (2014). doi:10.1063/1.4863748.

- [13] T.K. Liu, Z. Wu, A.D. Stoica, Q. Xie, W. Wu, Y.F. Gao, H. Bei, K. An, Twinning-mediated work hardening and texture evolution in CrCoFeMnNi high entropy alloys at cryogenic temperature, *Materials and Design*. (2017). doi:10.1016/j.matdes.2017.06.039.
- [14] T. Liu, Y. Gao, H. Bei, K. An, In situ neutron diffraction study on tensile deformation behavior of carbon-strengthened CoCrFeMnNi high-entropy alloys at room and elevated temperatures, *Journal of Materials Research*. (2018). doi:10.1557/jmr.2018.180.
- [15] D. Yu, K. An, X. Chen, H. Bei, Phase-specific deformation behavior of a NiAl-Cr(Mo) lamellar composite under thermal and mechanical loads, *Journal of Alloys and Compounds*. (2016). doi:10.1016/j.jallcom.2015.09.265.
- [16] S. Fu, Y. Chen, H. Bei, K. An, D. Yu, T.K. Liu, Deformation mechanisms and work-hardening behavior of transformation-induced plasticity high entropy alloys by in-situ neutron diffraction, *Materials Research Letters*. 6 (2018) 620–626. doi:10.1080/21663831.2018.1523239.
- [17] H. Huang, Y. Wu, J. He, H. Wang, X. Liu, K. An, W. Wu, Z. Lu, Phase-Transformation Ductilization of Brittle High-Entropy Alloys via Metastability Engineering, *Advanced Materials*. 29 (2017). doi:10.1002/adma.201701678.
- [18] Z. Li, C.C. Tasan, K.G. Pradeep, D. Raabe, A TRIP-assisted dual-phase high-entropy alloy: Grain size and phase fraction effects on deformation behavior, *Acta Materialia*. 131 (2017) 323–335. doi:10.1016/j.actamat.2017.03.069.
- [19] S. Sinha, S.S. Nene, M. Frank, K. Liu, R.S. Mishra, B.A. McWilliams, K.C. Cho, Microstructural Evolution and Deformation Behavior of Ni-Si- and Co-Si-Containing Metastable High Entropy Alloys, *Metallurgical and Materials Transactions A*. 50 (2018) 179–190. doi:10.1007/s11661-018-4968-6.
- [20] S. Wei, J. Kim, C.C. Tasan, Boundary micro-cracking in metastable Fe 45 Mn 35 Co 10 Cr 10 high-entropy alloys, *Acta Materialia*. 168 (2019) 76–86. doi:10.1016/j.actamat.2019.01.036.
- [21] Y. Bu, Z. Li, J. Liu, H. Wang, D. Raabe, W. Yang, Nonbasal Slip Systems Enable a Strong and Ductile Hexagonal-Close-Packed High-Entropy Phase, *Physical Review Letters*. 122 (2019) 75502. doi:10.1103/PhysRevLett.122.075502.
- [22] Z. Li, D. Raabe, Strong and Ductile Non-equiatomic High-Entropy Alloys: Design, Processing, Microstructure, and Mechanical Properties, *JOM*. 69 (2017) 2099–2106. doi:10.1007/s11837-017-2540-2.
- [23] S. Sinha, S.S. Nene, M. Frank, K. Liu, R.S. Mishra, B.A. McWilliams, K.C. Cho, Microstructural Evolution and Deformation Behavior of Ni-Si- and Co-Si-Containing Metastable High Entropy Alloys, *Metallurgical and Materials Transactions A: Physical Metallurgy and Materials Science*. 50 (2019). doi:10.1007/s11661-018-4968-6.
- [24] M. Kang, W. Woo, Y.K. Lee, B.S. Seong, Neutron diffraction analysis of stacking fault energy in Fe-18Mn-2Al-0.6C twinning-induced plasticity steels, *Materials Letters*. 76 (2012) 93–95. doi:10.1016/j.matlet.2012.02.075.
- [25] G. Meric de Bellefon, M.N. Gussev, A.D. Stoica, J.C. van Duysen, K. Sridharan,

- Examining the influence of stacking fault width on deformation twinning in an austenitic stainless steel, *Scripta Materialia*. 157 (2018) 162–166. doi:10.1016/j.scriptamat.2018.08.012.
- [26] K. An, VDRIVE Data Reduction and Interactive Visualization Software for Event Mode Neutron Diffraction, ORNL Report, 2012.
- [27] E.I. Galindo-Nava, P.E.J. Rivera-Díaz-del-Castillo, Understanding martensite and twin formation in austenitic steels: A model describing TRIP and TWIP effects, *Acta Materialia*. 128 (2017) 120–134. doi:10.1016/j.actamat.2017.02.004.
- [28] B.E. Warren, *X-Ray Diffraction*, 1990.
- [29] S. Harjo, Y. Tomota, P. Lukáš, D. Neov, M. Vrána, P. Mikula, M. Ono, In situ neutron diffraction study of α - γ Fe-Cr-Ni alloys under tensile deformation, *Acta Materialia*. (2001). doi:10.1016/S1359-6454(01)00147-1.
- [30] Z. Wang, A.D. Stoica, D. Ma, A.M. Beese, Diffraction and single-crystal elastic constants of Inconel 625 at room and elevated temperatures determined by neutron diffraction, *Materials Science and Engineering A*. (2016). doi:10.1016/j.msea.2016.08.010.
- [31] E. Cakmak, M.M. Kirka, T.R. Watkins, R.C. Cooper, K. An, H. Choo, W. Wu, R.R. Dehoff, S.S. Babu, Microstructural and micromechanical characterization of IN718 theta shaped specimens built with electron beam melting, *Acta Materialia*. (2016). doi:10.1016/j.actamat.2016.02.005.
- [32] T. Gnäupel-Herold, P.C. Brand, H.J. Prask, Calculation of Single-Crystal Elastic Constants for Cubic Crystal Symmetry from Powder Diffraction Data, *Journal of Applied Crystallography*. (1998). doi:10.1107/s002188989800898x.
- [33] M.A. Iadicola, T.H. Gnäupel-Herold, Effective X-ray elastic constant measurement for in situ stress measurement of biaxially strained AA5754-O, *Materials Science and Engineering A*. (2012). doi:10.1016/j.msea.2012.02.100.
- [34] T. Gnäupel-Herold, P.C. Brand, H.J. Prask, Accessing the elastic properties of cubic materials with diffraction methods, *Denver X-Ray Conference on Applications of X-Ray Analysis*. (2009). doi:10.4028/www.scientific.net/MSF.278-281.151.
- [35] J.R. Davis, *Nickel, Cobalt, and Their Alloys*, 2000. doi:10.1361/ncta2000p013.
- [36] T. Gebhardt, D. Music, D. Kossmann, M. Ekholm, I.A. Abrikosov, L. Vitos, J.M. Schneider, Elastic properties of fcc Fe-Mn-X (X = Al, Si) alloys studied by theory and experiment, *Acta Materialia*. (2011). doi:10.1016/j.actamat.2011.01.054.
- [37] R. Gaillac, P. Pullumbi, F.X. Coudert, ELATE: An open-source online application for analysis and visualization of elastic tensors, *Journal of Physics Condensed Matter*. (2016). doi:10.1088/0953-8984/28/27/275201.
- [38] W. Lu, C.H. Liebscher, G. Dehm, D. Raabe, Z. Li, Bidirectional Transformation Enables Hierarchical Nanolaminate Dual-Phase High-Entropy Alloys, *Advanced Materials*. 30 (2018). doi:10.1002/adma.201804727.

- [39] B.C. De Cooman, Y. Estrin, S.K. Kim, Twinning-induced plasticity (TWIP) steels, *Acta Materialia*. (2018). doi:10.1016/j.actamat.2017.06.046.
- [40] S.S. Nene, K. Liu, M. Frank, R.S. Mishra, R.E. Brennan, K.C. Cho, Z. Li, D. Raabe, Enhanced strength and ductility in a friction stir processing engineered dual phase high entropy alloy, *Scientific Reports*. 7 (2017). doi:10.1038/s41598-017-16509-9.
- [41] E.H. Kisi, C.J. Howard, *Applications of Neutron Powder Diffraction*, 2009. doi:10.1093/acprof:oso/9780198515944.001.0001.
- [42] G. Proust, G.C. Kaschner, I.J. Beyerlein, B. Clausen, D.W. Brown, R.J. McCabe, C.N. Tomé, Detwinning of high-purity zirconium: In-Situ neutron diffraction experiments, *Experimental Mechanics*. (2010). doi:10.1007/s11340-008-9213-6.
- [43] M. Frank, S.S. Nene, K. Liu, J. Reeder, R.S. Mishra, B.A. McWilliams, K. Cho, Z. Li, Dynamic Phase Stabilization in an Interstitial High Entropy Alloy upon Friction Stir Processing, *Manuscript Submitted*. (2019).
- [44] S. Harjo, N. Tsuchida, J. Abe, W. Gong, Martensite phase stress and the strengthening mechanism in TRIP steel by neutron diffraction, *Scientific Reports*. (2017). doi:10.1038/s41598-017-15252-5.
- [45] S.R. Agnew, D.W. Brown, C.N. Tomé, Validating a polycrystal model for the elastoplastic response of magnesium alloy AZ31 using in situ neutron diffraction, *Acta Materialia*. (2006). doi:10.1016/j.actamat.2006.06.020.
- [46] M.A. Gharghoury, G.C. Weatherly, J.D. Embury, J. Root, Study of the mechanical properties of Mg-7.7at.% Al by in-situ neutron diffraction, *Philosophical Magazine A: Physics of Condensed Matter, Structure, Defects and Mechanical Properties*. (1999). doi:10.1080/01418619908210386.
- [47] D.W. Brown, A. Jain, S.R. Agnew, B. Clausen, Twinning and Detwinning during Cyclic Deformation of Mg Alloy AZ31B, *Materials Science Forum*. (2009). doi:10.4028/www.scientific.net/msf.539-543.3407.
- [48] Z. Wu, W.A. Curtin, Mechanism and energetics of $\langle c + a \rangle$ dislocation cross-slip in hcp metals, *Proceedings of the National Academy of Sciences*. (2016). doi:10.1073/pnas.1603966113.
- [49] K.Y. Xie, Z. Alam, A. Caffee, K.J. Hemker, Deformation behavior of Mg single crystals compressed along c-axis, in: *Magnesium Technology 2016*, 2016. doi:10.1002/9781119274803.ch42.
- [50] N. Dixit, K.Y. Xie, K.J. Hemker, K.T. Ramesh, Microstructural evolution of pure magnesium under high strain rate loading, *Acta Materialia*. (2015). doi:10.1016/j.actamat.2014.12.030.
- [51] K.Y. Xie, Z. Alam, A. Caffee, K.J. Hemker, Pyramidal slip in c-axis compressed Mg single crystals, *Scripta Materialia*. (2016). doi:10.1016/j.scriptamat.2015.09.016.
- [52] X.L. Nan, H.Y. Wang, Z.Q. Wu, E.S. Xue, L. Zhang, Q.C. Jiang, Effect of c/a axial ratio on Schmid factors in hexagonal close-packed metals, *Scripta Materialia*. (2013).

doi:10.1016/j.scriptamat.2012.12.006.

- [53] X.L. Nan, H.Y. Wang, L. Zhang, J.B. Li, Q.C. Jiang, Calculation of Schmid factors in magnesium: Analysis of deformation behaviors, *Scripta Materialia*. (2012).
doi:10.1016/j.scriptamat.2012.05.042.